Phys. Status Solidi B **253,** No. 9, 1771–1781 (2016) / **DOI** 10.1002/pssb.201600134

physica status solidi b
www.pss-b.com
basic solid state physics

Magnetoelectric and magnetoresistive properties of the $Ce_xMn_{1-x}S$ semiconductors

S. S. Aplesnin[1,2], M. N. Sitnikov[2], O. B. Romanova[*,1], and A. Yu. Pichugin[3]

[1] Kirensky Institute of Physics SB RAS, Akademgorodok 50, 660036 Krasnoyarsk, Russia
[2] Siberian State Aerospace University M F Reshetnev, Krasnoyarsky Rabochy Av. 31, 660014 Krasnoyarsk, Russia
[3] Nikolaev Institute of Inorganic Chemistry SB RAS, Acad. Lavrenntiev Ave. 3, 630090 Novosibirsk, Russia

Received 17 March 2016, accepted 20 April 2016
Published online 11 May 2016

Keywords dielectric permeability, Hall effect, magnetoelectric properties, magnetoresistive properties, semiconductors

* Corresponding author: e-mail rob@iph.krasn.ru, Phone: +39 12 907108, Fax: +39 12 438923

The effect of electron doping on the magnetoelectric and magnetoresistivity properties of cation-substituted antiferromagnetic $Ce_xMn_{1-x}S$ ($x \leq 0.05$) semiconductors at temperatures of 77–500 K in magnetic fields of up to 10 kOe was investigated. For all the compositions shifts of the temperature of the dielectric loss maximum toward higher temperature (80–500 K) with increasing magnetic field up to 10 kOe are found. The current dependence of magnetoresistance from the *I–V* characteristic measured in a magnetic field was established. The increase of the magnetoresistive effect with increase of the cerium ions concentration in the $Ce_xMn_{1-x}S$ is found. The type of current carriers was determined on the basis of the Hall coefficient measurement. For explanation of experimental data the model of charge-orbital ordering, including orbital glass is used.

1 Introduction Much attention is currently focused upon studying the materials with a strong interplay of electrical and magnetic properties, which are promising for application in microelectronics [1, 2]. Magnetoresistance in the paramagnetic region can be caused by the presence of degenerate electronic orbital states and strong electron correlations [3]. Depending on orbital occupancies, the electronic orbital states of different types, including incommensurate ones [4], can be induced [5, 6]. The orbital ordering can be accompanied by the lattice distortion and Jahn–Teller coupling between electrons and the lattice.

At a certain doping concentration, the disordered orbital state can be established due to local lattice strains. Analogously to the case of disordered spin systems with ferromagnetic polarons in the paramagnetic region [7], the kinetic properties of such systems at high temperatures are affected by orbital polarons [8]. In the presence of the orbital magnetic moment of, e.g., electrons in the t_{2g} states, the orbital polarons have a magnetic moment. In this case, the orbital polaron energy depends on the direction and value of the external magnetic field and the magnetoresistive effect can be observed.

The degenerate states of manganese ions Mn^{2+} with the $3d^5$ configuration can be obtained by electron doping to the 3d band, in particular, by substitution of divalent cobalt with the $3d^7$ configuration for divalent manganese. The degeneracy is eliminated by the strong electron correlations, which are taken into account in studying the transport and magnetic properties of the $Co_xMn_{1-x}S$ solid solution [9, 10]. The threefold degeneracy of the t_{2g} states is eliminated after the formation of the doublet $d_{\beta\alpha}$, d_γ (β, α, $\gamma = xy$, zx, zy) at ~500 K. The degeneracy of the d_α and d_β orbitals is eliminated with decreasing temperature at ~240 K [11].

Substitution of a trivalent 4f ion, e.g., cerium, for Mn^{2+} in low concentrations ($x < 0.05$), when the interaction between cerium ions can be ignored, induces not only orbital degeneracy, but also charge ordering with the formation of defects in accordance with the anion system. In this case, donor and acceptor doping occurs.

Manganese and cerium sulfides have a fcc lattice of the NaCl type with the lattice parameters $a = 0.5222$ nm (MnS) [12] and 0.5777 nm (CeS) [13]. Cerium sulfide is characterized by metal-type conductivity and at low temperatures passes to the magnetically ordered antiferromagnetic state with the Néel temperature $T_N = 4$ K and the effective

magnetic moment $m = 2.78\ \mu_B$ [14]. According to the results of the theoretical calculations, the 4f level lies above the bottom of the conduction band in CeS and the ionic radius of cerium is the largest among all 4f elements [15].

Previously, the magnetoresistive effect in the paramagnetic region was observed in the $Gd_xMn_{1-x}S$ solid solution [16]. Gadolinium sulfide is also a metal, whose resistivity is lower than the resistivity of CeS by a factor of 3 and the lattice constant is smaller than that of CeS by 5%. The electronic structures of cerium and gadolinium ions are strongly different. The gadolinium ion is in the *s* state; in cerium, the spin–orbit interaction attains 0.5 eV. The energy difference between the di- and trivalent states in sulfides is 2.5 eV for cerium and 3.8 eV for gadolinium [15]. This is related to the position of the 4f level relative to the bottom of the conduction band. In manganese sulfide, the position of the 4f level in the bandgap in the presence of donor and acceptor levels will determine the position of the chemical potential and, consequently, the kinetic properties. The next moment is related to the effect of 4f ions on the nearest manganese ions. Since the cerium ion has the large ionic radius, the chemical pressure changes the crystal field, charge gap, and hybridization of valence bonds between manganese ions and between manganese and 4f elements.

The aim of this study was to establish the correlation between the dynamic magnetic, dielectric and transport properties in the magnetic fields for solid solutions $Ce_xMn_{1-x}S$ upon electron doping.

2 Dynamic magnetic properties The $Ce_xMn_{1-x}S$ with concentration ($0.01 \le x \le 0.05$) samples were synthesized from the melt [17]. A charge for melting and melt crystallization was prepared by thorough mixing of calculated amounts of polycrystalline manganese sulfide obtained by sulfidizing of ultrapure manganese dioxide and polycrystalline cerium monosulfide. Crystallization occurred at temperatures starting from about 1900 K. Sublimation was not observed; therefore, the crystal composition does not depend on the filling. The completeness of the sulfidizing process was controlled by X-ray diffraction analysis and a weighing technique.

The prepared samples were studied on JEOL JSM 6700 F and Hitachi TM3000 scanning electron microscopes with an EDAX analytical device. In the investigations, crystal cleavages and powders for the XRD analysis were used. In microphotographs, cerium-doped manganese sulfide crystal cleavages are homogeneous, except for the composition with $x = 0.1$. The measurement results for this $x = 0.1$ is not presented in this article. The X-ray structural analysis of the $Ce_xMn_{1-x}S$ sulfides ($0.01 \le x \le 0.05$) was performed on a DRON-3 diffractometer (CuK_α radiation) at a temperature of 300 K. X-ray diffraction patterns for the compositions with $x = 0.01$, 0.03, and 0.05 (Fig. 1a–c) are presented. According to the X-ray diffraction patterns $Ce_xMn_{1-x}S$ ($0.01 \le x \le 0.05$) have a face-centered cubic (fcc) lattice of NaCl, typical of MnS. As the degree of cation substitution (X) is increased 5.222 Å ($x = 0$) to 5.228 Å ($x = 0.05$), lattice

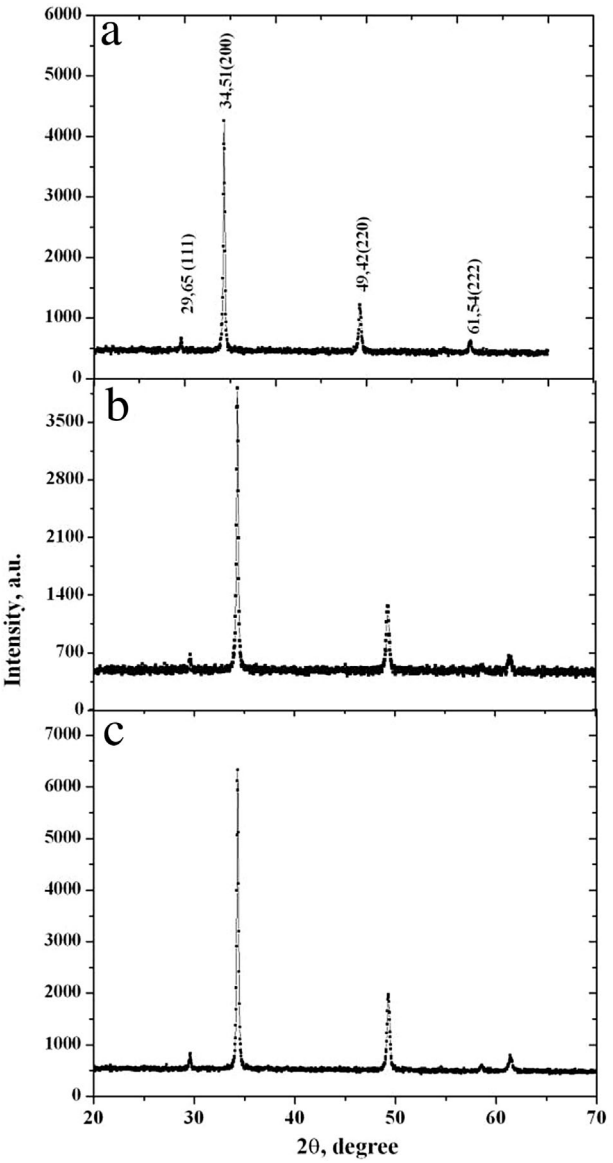

Figure 1 X-ray diffraction pattern of the $Ce_{0.01}Mn_{0.99}S$ (a), $Ce_{0.03}Mn_{0.97}S$ (b), and $Ce_{0.05}Mn_{0.95}S$ (c) samples at room temperature.

parameter *a* grows linearly, indicating the formation of solid solutions.

The specific magnetization and magnetic susceptibility were determined by the Faraday technique in a magnetic field $H = 8.6$ kOe in the temperature range $80\ K < T < 1000\ K$. The temperature dependence of the magnetic susceptibility in the heating–cooling regime for one of the compositions is presented in Fig. 2.

The temperature dependence of the susceptibility reveals the susceptibility maxima at the temperatures T ($x = 0.01$) = 162 K, T ($x = 0.03$) = 164 K, and T ($x = 0.05$) = 155 K. The hysteresis curve of the magnetization in magnetic fields up to 90 kOe for $x = 0.01$ and nonlinear field behavior at $T < 8\ 0$ K and linear above 80 K of the

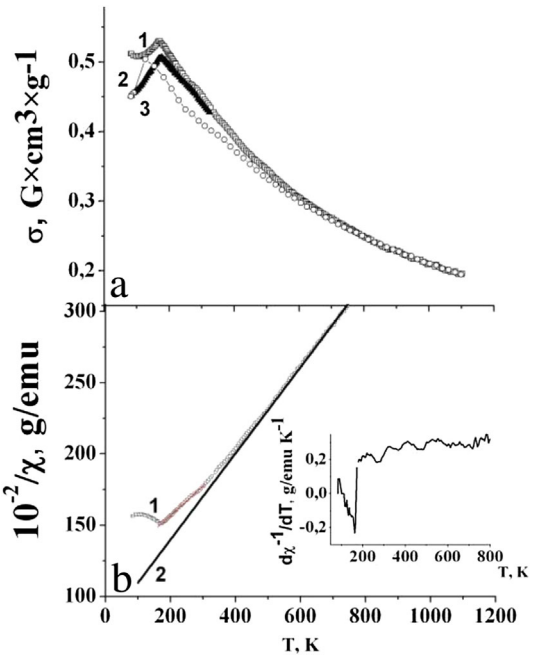

Figure 2 (a) Magnetization of the $Ce_{0.03}Mn_{0.97}S$ sample upon (1) heating, (2) cooling, and (3) repeated heating to 300 K in the magnetic field $H = 8.6$ kOe. (b) Inverse susceptibility versus temperature. Inset: temperature derivative of the inverse susceptibility.

magnetization for $x = 0.05$ the sharp Curie temperature drop were found and were presented in Ref. [18]. In the high-temperature region, the deviation from the Curie–Weiss law at $T \sim 500$ K and the inflection of $1/\chi(T)$ at $T = 260$ K are observed. For the composition with $x = 0.03$, the derivative $d(1/\chi(T))/dT$ is minimum at the temperatures $T = 262$ and 473 K (inset to Fig. 2). Upon cooling in a magnetic field (FC mode), the susceptibility decreases and its maximum shifts to the temperature $T = 140$ K. Electron doping leads to degeneracy of the t_{2g} states of manganese ions, which is eliminated by the Coulomb interaction with splitting of multiplets by states $d_{\alpha,\beta}$ and d_{γ} with the orbital moment projection $L^z = -1,\ 0,\ +1$. The correlation of orbital moments is implemented by the spin–orbit interaction at electron hopping and by the Jahn–Teller effect with lowering of the local symmetry of crystal field. As the temperature is decreased, the t_{2g} states are three-fold split in the range 220–260 K. The electronic structure variation on the manganese ion induces strain or rotation of sulfur octahedra and partial localization of holes, which leads to the variation in the exchange coupling value and to the magnetic susceptibility anomaly.

In the $Ce_xMn_{1-x}S$ compounds, the effective exchange coupling parameter $J = J_s + J_m \langle L(0)L(h)\rangle$ is determined by the correlation function of orbital angular momenta between nearest neighbors ($\langle L(0)L(h)\rangle$) and exchange coupling between the spin and orbital moments (J_m). At low concentrations, the magnetic structure of the orbital moments is incommensurate with the degeneracy by the wave vector of the structure, which can be schematically presented as $\langle\uparrow\uparrow\uparrow\uparrow\downarrow\downarrow\downarrow\downarrow\rangle$ and $\langle\uparrow\uparrow\uparrow\downarrow\downarrow\downarrow\downarrow\rangle$. In a magnetic field, the longitudinal component of the orbital moment directed opposite to the field decreases and the correlator ($\langle L^z(0)\ L^z(h)\rangle$) increases due to rearrangement of the orbital structure; e.g., $\langle\uparrow\uparrow\uparrow\uparrow\downarrow\downarrow\downarrow\rangle$. At the negative sign of the interaction between the spin and orbital moments, the absolute value of the exchange coupling increases and the magnetic susceptibility decreases, since near the Néel temperature the magnetic susceptibility is $\chi \sim 1/J$. The susceptibility ratio at $J_m\langle L^z(0)\ L^z(h)\rangle \ll J_s$ can be presented in the form

$$\frac{\chi^{ZF}(T_N)}{\chi^{FC}(T_N)} = \frac{(1 + \lambda\langle L^z(0)L^z(h)\rangle^{FC})}{(1 + \lambda\langle L^z(0)L^z(h)\rangle^{ZF})} = 1 + \lambda(\langle L^z(0)L^z(h)\rangle^{FC} - \langle L^z(0)L^z(h)\rangle^{ZF}), \quad (1)$$

where $\lambda = J_m/J_s$ and $\langle L^z(0)\ L^z(h)\rangle^{FC,ZF}$ is the correlator of the orbital moments cooled in the FC and ZFC modes. The relative variation in the susceptibility of the samples cooled in the FC and ZFC modes near T_N is 5%. The growth of the orbital correlator upon FC can attain 50% at the parameters $J_m \approx J_s$ and $\langle L^z(0)\ L^z(h)\rangle^{ZF} = 0.1$. The orbital correlation function is smaller than the correlation function between nearest neighbors near the Néel temperature $\left|\langle S^z(0)\ S^z(h)\rangle\right| \approx 1$ for the manganese ion spins $S = 5\,\mu_B$ by more than an order of magnitude [19]. In the magnetically ordered region, the spin–orbit interaction rearranges the orbital order, the incommensurability vector $q = Q_o - Q_{AF}$ between the orbital (Q_o) and spin (Q_{AF}) ordering decreases, and the effective exchange coupling increases, which results in the Néel temperature growth. Indeed, upon repeated heating, the susceptibility maximum shifted to the right by 8 K to $T_N^F = 172$ K, which implies an increase in the exchange by 4.4%.

The dynamic characteristics of the magnetic and dielectric subsystems and the effect on the magnetodielectric properties will be determined from the inductance of a multilayer coil consisting of 10 000 turns of a copper wire with an inner diameter $d = 2$ mm and a length of 10 mm, inside which the sample was placed. The measurements were performed in the frequency range $0.1 < \omega < 100$ kHz. The inductances of the coil with the sample (L_f) and without it (L_s) were measured, since the inductance of a solenoid is proportional to $L = n^2\mu\mu_0 V$ and the magnetic susceptibility of the sample with volume V_f is proportional to $(L_f - L_s)/L_s$. In addition, the multilayer coil is characterized by a capacitance resistance. Therefore, the measured inductance depends not only on permeability, but also on permittivity. The magnetic contribution can be separated by comparing the measured inductance and capacitance. We measured the inductance on an AM-3028 component analyzer and hereinafter use the term the relative inductance variation: $\delta L(T) = (L_f - L_s)/L_s$.

The relative inductance variation for the composition with $x = 0.01$ with temperature (Fig. 3) has a maximum near the Néel temperature. The temperature of this maximum increases with frequency from $T_{max} = 123$ K at $\omega = 0.1$ kHz to 136 K at $\omega = 1$ kHz in accordance with the power law $T_{max} = A\omega^n$ with $n = 0.023(3)$, which is typical of orbital glasses. Upon cooling in a magnetic field, the distance step-wise decreases at the temperatures $T = 141$ K ($\omega = 0.1$ kHz), 140 K ($\omega = 1$ kHz), and 139 K ($\omega = 10$ kHz). Below the Néel temperature, the electronic structure of the t_{2g} multiplets with the orbital moment projections $L^z = \pm 1$ is rearranged due to the interaction between spin and orbital moments. At the concentration $x = 0.03$ (Fig. 3), the maximum inductance temperature lies within 136–139 K and the inductance of the coil with the sample cooled in zero field at the frequency $\omega = 0.1$ kHz is maximum at the temperature $T = 118$ K. The shift of $\delta L(T)$ to the low-temperature region and disappearance of the jump are related to the variation in the wave vector of orbital ordering (Q_o) and a decrease in the incommensurability vector $q = Q_o - Q_s$ between the orbital and spin ordering (Q_s).

At frequencies $\omega < 10$ kHz, the inductance of the coil with the sample cooled in a magnetic field exceeds that of the coil with the sample cooled in zero field with a decrease in temperature from $T = 300$ K. The difference between these inductances is maximum at $T \approx 270$ K and decreases by two orders of magnitude (to 0.4%) for the composition with $x = 0.05$. The compositions with $x = 0.01$ and 0.03 are characterized by the spin-glass behavior. This phenomenon is attributed to elimination of degeneracy of the orbital angular momenta in a magnetic field, separation of the magnetic anisotropy axis in the crystal, and an increase in the contribution of the orbital angular momentum to the magnetic susceptibility. For the composition with $x = 0.05$, the inductance jump occurs in the region of structural lattice distortion observed in MnS at $T = 165$ K [20]. In nonequilibrium systems, the relaxation time is frequency dependent. The relaxation frequency can be determined form the Q factor: $Q = \omega\tau/2$, i.e., $\tau = 2Q/\omega$. The Q factor of electromagnetic oscillations of the coil is presented in Fig. 4. At low frequencies ($\omega = 0.1$–10 kHz), the relaxation time is frequency independent. The time of relaxation of electromagnetic oscillations in the coil with the sample grows step-wise in the low-frequency region upon cooling the $Ce_{0.01}Mn_{0.99}S$ sample in the magnetic field $H = 2.5$ kOe below the Néel temperature at $T < 138$ K, except for the relaxation at the frequency $\omega = 10$ kHz. For the composition with $x = 0.03$, the relaxation time also increases in a magnetic field at $T < 134$ K (Fig. 4b). In the temperature range 220–300 K, the Q factor (relaxation time) decreases in a magnetic field by 10–14% for the compositions with $x = 0.01$ and 0.03 at the frequencies $\omega < 50$ kHz. In the $Ce_{0.05}Mn_{0.95}S$ compound, the Q-factor jump is observed at the frequency $\omega = 10$ kHz in a magnetic field 2.5 kOe at

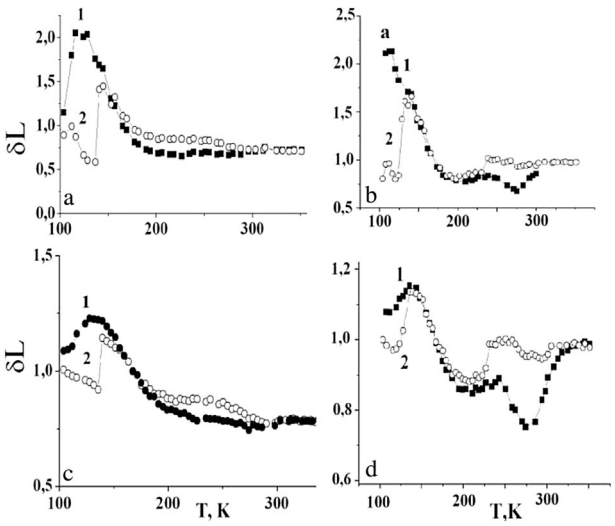

Figure 3 Temperature dependence of the relative inductance variation ($\delta L(T) = (L_f - L_s)/L_s$) of the coil with ($L_f$) and without a sample ($L_s$) measured upon cooling in zero magnetic field (1) and in the magnetic field $H = 2.5$ kOe (2) for the composition with $x = 0.01$ at $\omega = 0.1$ kHz (a) and 1 kHz (b). At $\omega = 0.1$ kHz (c) and 1 kHz (d) for the $Ce_{0.03}Mn_{0.97}S$ sample.

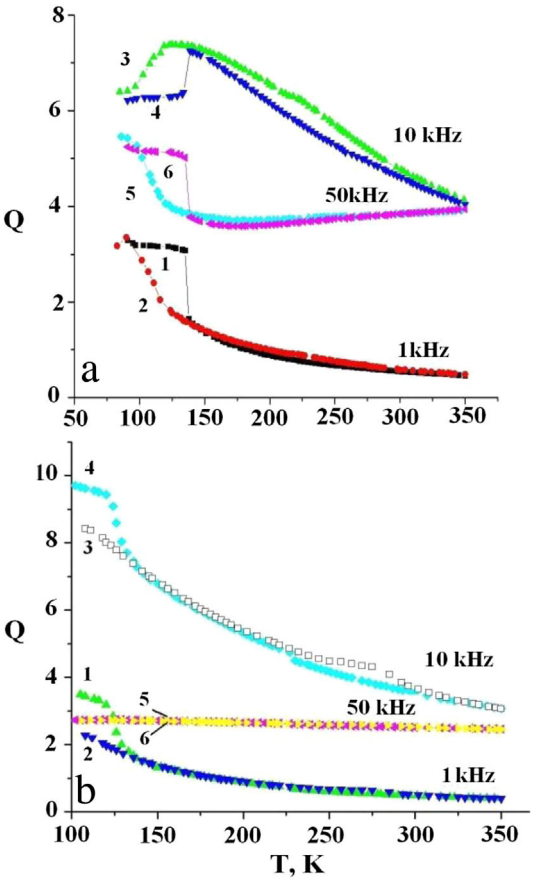

Figure 4 Temperature dependence of the Q factor of the coil with the sample cooled in zero field (2,3,5) and in the magnetic field 2.5 kOe (1,4,6) at $\omega = 1$ kHz (1,2), 10 kHz (3,4), and 50 kHz (5,6) for the $Ce_xMn_{1-x}S$ sample with $x = 0.01$ (a) and 0.03 (b).

$T = 134$ K; below this temperature, the Q factor increases in a magnetic field, while above this temperature it decreases up to 300 K.

The variation in the time of relaxation of electromagnetic oscillations depends on temperature and frequency and the qualitative behavior of $\tau(\omega, H)$ can be described using the model of damped electromagnetic oscillations. The resonance frequency of the oscillatory circuit (coil with the sample) is $\omega^2_r = \omega^2_0 - \beta^2 = 1/LC - R^2/4L^2$ and the Q factor is $Q = A_r/A_s$, where A_r is the resonance amplitude of oscillations and A_s is the amplitude of oscillations far from resonance. Upon cooling the sample in a magnetic field, the inductance decreases and the resonance frequency increases; correspondingly, the frequency at which the Q factor is measured shifts from the resonance frequency (ω–ω_r) and the amplitude $A_s(\omega$–$\omega_r)$ decreases. The ratio between the Q factors is $Q_H/Q_{H=0} = A_s(H=0)/A_s(H) > 1$ at $\omega < \omega_r$ and $A_s(H=0)/A_s(H) < 1$ at $\omega > \omega_r$.

For the compositions with $x = 0.01$ and 0.03, the slope of the temperature dependence of the relaxation frequency changes in the temperature range 220–230 K and for the composition with $x = 0.05$, at $T = 168$ K, where the resistivity is maximum. The temperature dependence of the relaxation time is maximum at $T = 170$ K for the composition with $x = 0.01$ at a frequency of 50 kHz, where dielectric loss and magnetoresistance anomalies are observed.

Thus, the anomalies in the temperature dependence of the inductance and Q factor of electromagnetic oscillations of the coil with the sample below the Néel temperature in a magnetic field are caused by the spin–orbit interaction and rearrangement of the orbital and spin structures, while at higher temperatures, they result from elimination of degenerate orbital states in a magnetic field.

3 Magnetoelectric properties The dielectric properties of semiconductors are described by permittivity and dipole moment relaxation, which are determined from the capacitance and dissipation factor. Knowing the permittivity value, one can establish the occurrence of structural transitions and metal–dielectric transitions in semiconductors. In addition, the dielectric properties provide information about charge transport and charge ordering. Upon approaching the metal–dielectric transition from the dielectric phase side, a decrease in the resistivity is accompanied by an increase in the permittivity, which was observed in some doped semiconductors [21, 22]. Therefore, it is not excluded that the electronic system contributes to the permittivity.

The response of the dielectric properties to the magnetic field makes it possible to establish the main mechanisms that determine the behavior of the dielectric and electric transport properties. The permittivity was determined from the capacitance measured with an AM-3028 LCR Meter at the frequency $\omega = 100$ kHz in the temperature range $100\text{ K} < T < 450\text{ K}$. Figure 5 shows the real part of permittivity for the samples of three compositions cooled

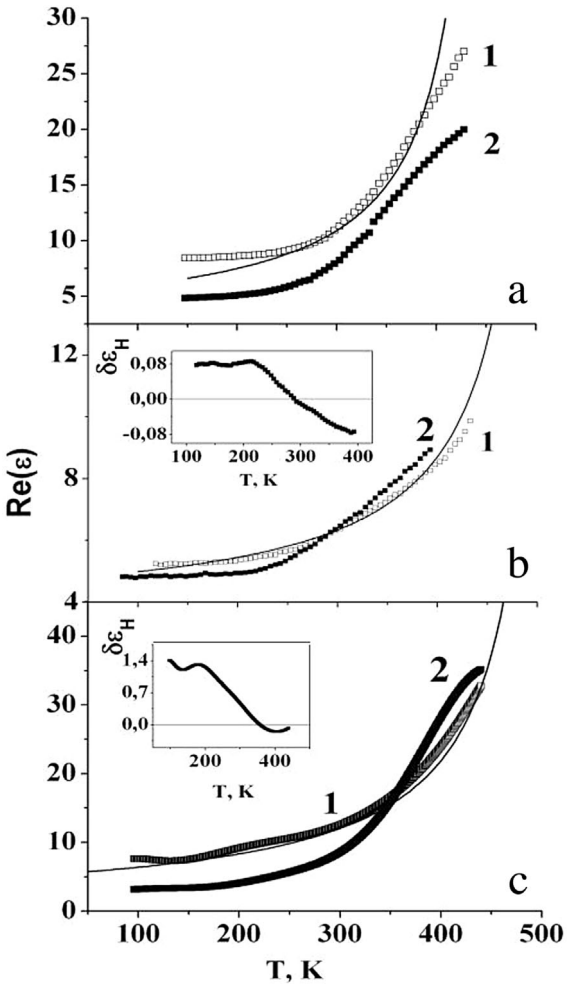

Figure 5 Temperature dependence of the real part of the permittivity of the $Ce_xMn_{1-x}S$ samples cooled in the magnetic field $H = 8$ kOe (1) and in zero magnetic field (2) at the frequency $\omega = 100$ kHz for $x = 0.01$ (a), 0.03 (b), and 0.05 (c). Insets to (b, c): temperature dependence of the permittivity $\delta\varepsilon_H = (\varepsilon(H) - \varepsilon(0))/\varepsilon(0)$ in a magnetic field. The fitting function $\mathrm{Re}(\varepsilon) = A/(1 - T/T_0)$ is shown by a solid line.

in the ZFC mode and in the field $H = 8$ kOe as a function of temperature. In the low-temperature region, Re(ε) weakly depends on temperature and sharply ascends above 250–300 K, similar to the dc conductivity. In a magnetic field, the permittivity increases, while the magnetic capacitance decreases and, with an increase in temperature, passes through the minimum at $T = 350$ K for the composition with $x = 0.01$, changes its sign for negative at $T = 300$ and 350 K for the compositions with $x = 0.03$ and 0.05, respectively, and vanishes at high temperatures.

The electric charge can be compensated at low electron doping concentrations due to nonstoichiometry of sulfur ions with the formation of holes. Localization of electrons on the t_{2g} orbitals in the range 440–500 K due to the orbital ordering near cerium ions lowers the symmetry

of the electron density distribution and induces charge localization. We present the polarization in the form $P = el = e\xi = \chi\varepsilon_0 E$, where ξ is the radius of charge localization and χ is the dielectric susceptibly determined by charge fluctuations: $\chi \sim \xi = A/(1 - T/T_0)^{\nu}$, where T_0 is the critical temperature of orbital glass and $\nu = 1$ is the correlation radius exponent. In a magnetic field, the electron localization plane is oriented such that the orbital angular momentum will be codirected with the field, which leads to an increase in temperature T_0 due to weakening of elastic strains and lowering of the domain-wall density. This will cause the polarization growth and, consequently, an increase in the permittivity. The functional relation $\chi \sim \xi$(T) qualitatively describes the change in the temperature behavior of permittivity (lines in Fig. 5) in a magnetic field with the temperatures $T_0(x = 0.01) = 460$ K, $T_0(x = 0.03) = 480$ K, and T_0 $(x = 0.05) = 480$ K. In zero magnetic field, the dependence $\varepsilon(T)$ attains its maximum at 440–470 K. The permittivity variation with temperature cannot be described by the plasmon contribution of conduction electrons at the Fermi level $\varepsilon_p = ne^2/m^*\omega^2$, where n is the electron concentration, e is the elementary charge, and m^* is the effective mass. In particular, it can be seen that the permittivity ratios exceed the conductivity variations at the given temperatures by an order of magnitude: $\varepsilon(T = 450\,\text{K})/\varepsilon(T = 150\,\text{K}) = 4$, $\sigma(T = 450\,\text{K})/\sigma(T = 150\,\text{K}) = 0.06$ at $x = 0.01$; $\varepsilon(T = 400\,\text{K})/\varepsilon(T = 150\,\text{K}) = 2$, $\sigma(T = 400\,\text{K})/\sigma(T = 150\,\text{K}) = 0.25$ at $x = 0.03$; and $\varepsilon(T = 450\,\text{K})/\varepsilon(T = 150\,\text{K}) = 10$, $\sigma(T = 450\,\text{K})/\sigma(T = 150\,\text{K}) = 0.2$ at $x = 0.05$. This model explains the change in the magnetic capacitance sign with increasing temperature and yields the critical temperature at which the magnetic capacitance vanishes.

The imaginary part of permittivity characterizes the loss of electromagnetic radiation to the ion or electron subsystem and is determined by the dissipative factor $\text{tg}\delta = \text{Im}(\varepsilon)/\text{Re}(\varepsilon)$. For all the compositions, the dielectric loss maximum is observed (Fig. 6), which shifts toward higher temperatures with increasing magnetic field from $T = 370$ K at $H = 0$ to $T = 432$ K at $H = 2.5$ kOe due to the ordering of orbital angular moment. Near the temperature of the structural variation from the cubic to rhombohedral lattice at $T = 168$ K, the dielectric loss increases in a magnetic field. This is caused by elimination of the fourfold degeneracy of the rhombohedral distortion axis in a magnetic field and a decrease in the domain-wall density. The relaxation time in a ferroelectric system is $\tau \sim 1/(1 - T/T_0)^{z\nu}$, where $z\nu$ are the critical indices and decreases with increasing critical temperature, since at a fixed temperature $T_0(H)/T_0$ $(H = 0) > 1$ and τ $(H) < \tau$ $(H = 0)$.

As the cerium ion concentration is increased, the maximum of the imaginary part of permittivity shifts to the high-temperature region to $T = 427$ K at $x = 0.03$ and to $T = 430$ K at $x = 0.05$ in a zero magnetic field. In a magnetic field, one can also observe the shift of the Im($\varepsilon(T)$) maximum temperature toward higher temperatures:

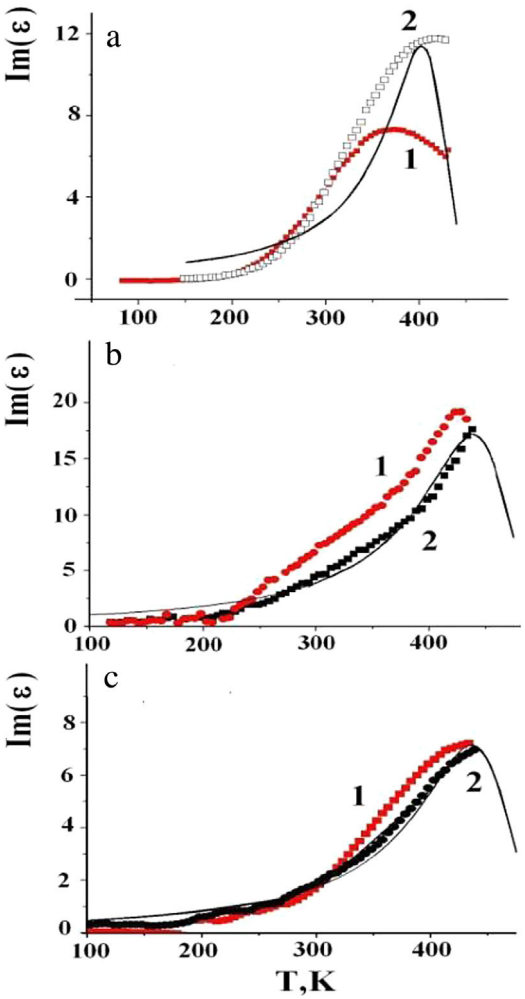

Figure 6 Temperature dependence of the imaginary part of the permittivity of the $Ce_xMn_{1-x}S$ samples cooled without magnetic field (1) and in the magnetic field $H = 8$ kOe (2) at $\omega = 100$ kHz for $x = 0.01$ (a), 0.03 (b), and 0.05 (c). The fitting function is Im $\chi = \chi_0(\omega\tau)/(1 + (\omega\tau)^2)$, where $\tau = \tau_0/(1 - T/T_0)^2$ is shown by the solid line.

$T = 404$ K at $x = 0.01$ to $T = 430$ K at $x = 0.03$ and 0.05. These maxima at the frequency $\omega = 100$ kHz are caused by the coinciding relaxation and measuring times and can be described using the Debye model

$$\text{Im}\chi = \frac{\chi_0(\omega\tau)}{\left(1 + (\omega\tau)^2\right)},$$

$$\tau = \frac{\tau_0}{(1 - T/T_0)^{z\nu}}, \qquad (2)$$

where χ_0 is the steady-state susceptibility and τ_0 is the frequency factor determining the relaxation in the low-temperature region $T \ll T_0$. In Fig. 6, the fitting function with $z\nu = 2$ satisfactorily describes the experimental data in a wide temperature range with the temperatures at which the

dielectric susceptibility is maximum; the relaxation frequency at low temperatures lies in the megahertz frequency range $\omega_r \sim 10$ MHz: in a magnetic field, $\tau_0 = 1.5 \times 10^{-7}$ s at $x = 0.01$, $\tau_0 = 1.6 \times 10^{-7}$ s at $x = 0.03$, and $\tau_0 = 2.1 \times 10^{-7}$ s at $x = 0.05$. The relaxation time is typical of domain walls in ferroelectrics [23].

The relative dielectric loss variation in a magnetic field $\delta\mathrm{Im}(\varepsilon) = [\mathrm{Im}(\varepsilon(H)) - \mathrm{Im}(\varepsilon(0))]/\mathrm{Im}(\varepsilon(0))$ is determined. The magnetic field induces a small peak of the imaginary part of permittivity in the temperature range $T_1 = 165$–180 K for all the compositions; at $T_2 = 220$ K, an additional maximum is observed for the compositions with $x = 0.03$ and 0.05. At T_1 and T_2, the degeneracy of the orbital angular momentum direction is eliminated in a magnetic field. An increase in the dielectric loss in a magnetic field below the Néel temperature is associated with the spin–orbit interaction, since the wave vector of orbital correlations changes upon sample cooling in the FC mode. In this case, the dielectric loss is determined by the magnetoelectric interaction and energy transfer to the magnetic subsystem.

4 Magnetoresistive properties The electrical resistivity of the $Ce_xMn_{1-x}S$ solid solutions was measured by a four-probe technique on the samples cooled in the ZFC mode and on the samples cooled and heated in the field $H = 8$ kOe. The temperature dependences of resistivity for the compositions with $x = 0.01$, and 0.05 are presented in Ref. [18].

Upon zero field cooling, the observed resistivity maximum shifts toward lower temperatures with increasing concentration: from $T = 238$ K for $x = 0.01$ and $T = 200$ K for $x = 0.03$ to $T = 166$ K for $x = 0.05$. Below the maximum temperature, the resistivity weakly changes in a certain temperature range and its value is smaller by several times than that at room temperature. In the magnetic field $H = 8$ kOe, the maximum of the temperature dependence of resistivity shifts by 72 K to $T = 166$ K at $x = 0.01$ and by 65 K to $T = 134$ K at $x = 0.03$; for the composition with $x = 0.05$, the temperatures coincide, but the resistivity value in a magnetic field doubles at room and higher temperatures and increases by 300–500% at low temperatures. The shift of the resistivity maximum results in the change of the magnetoresistance sign from positive to negative (Fig. 7).

The resistivity of the samples cooled in zero field remains invariable during passing through the antiferromagnet–paramagnet magnetic phase transition. In the magnetically ordered region, the resistivity of $Ce_{0.01}Mn_{0.99}S$ is constant and decreases smoothly in the temperature range 124–134 K for the composition with $x = 0.03$ and step-wise at $T = 125$ K for $x = 0.05$. At these temperatures, no anomalies were observed in the magnetic characteristics, which is apparently due to the crystal lattice strain.

In the samples cooled and heated in a magnetic field, the resistivity increases below the Néel temperature at $T(x = 0.01) = 130$ K, and $T(x = 0.03) = 133$ K and jumps at $T(x = 0.05) = 132$ K. These temperatures are below the

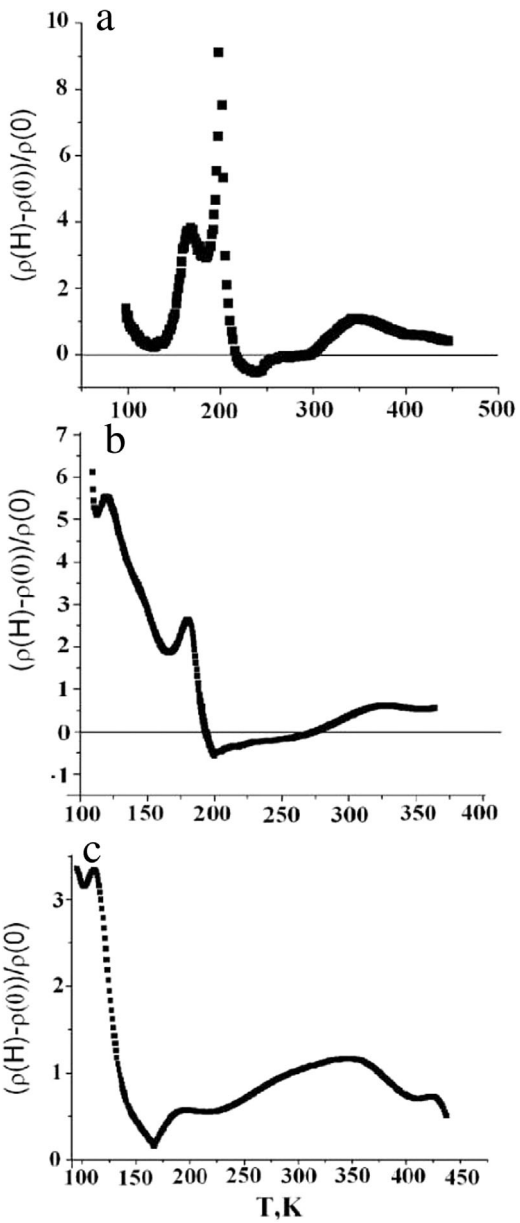

Figure 7 Temperature dependence of the relative resistivity variation $(\rho(H)-\rho(0))/\rho(0)$ for samples $Ce_xMn_{1-x}S$ with $x = 0.01$ (a), 0.03 (b), and 0.05 (c).

temperatures of the magnetic inductance maximum by 6–8 K. The absence of changes in conductivity at the Néel temperature is due to the hole conduction type on sulfur ions. The hole is not sensitivity to the magnetic order.

At temperatures below 300 K for all compositions the conductivity can be described by tunneling electrons and holes. The probability of tunneling of particles through the potential barrier depends on the barrier thickness and height and on the effective mass of particles. The main factor in a decrease in the tunneling constant is the variation in the carrier effective mass $(\delta_t^R/\delta_t^c)^2 = m_R^*/m_C^*$, which amounts to $m_R^*/m_C^* = 0.88$ for $x = 0.05$. For the compositions with

$x = 0.01$ and 0.03, the electronic structure rearrangement at temperature T_{Rm} corresponding to the observed anomalies in magnetic characteristics leads to the change in the effective mass by 20% for $x = 0.01$ and 31% for $x = 0.03$. In the low-temperature region, the effective mass increases in a magnetic field: $m^*(H)/m^*(0) = 1.05$ at $x = 0.01$, 1.06 at $x = 0.03$, and 1.18 at $x = 0.05$. The rhombohedral lattice distortion leads to a decrease in width W of the localized state band and, consequently, to an increase in the effective mass $m^* \sim 1/W$. As a result, the degeneracy of multiplets with the orbital moment projections $L^z = \pm 1$, which equiprobably occupy the upper and lower energy levels, is eliminated. The applied magnetic field determines the orientation of the distortion of a tetrahedron along one of the cube spatial diagonals and leads to redistribution of multiplets due to the Zeeman interaction energy $H\,L^z$. In a magnetic field, the width W of the localized state decreases with a decrease in the dispersion of rhombic distortion axes and the carrier effective mass increases. Upon further heating in a magnetic field above 500 K, the orbital glass vanishes, the width of the spectral density of localized electron states increases, the effective mass decreases, and the dependence on the magnetic field disappears.

Figure 8 shows room-temperature I–V characteristics with and without a field. As the voltage is increased, the current monotonically grows and at $U_c > 1.2$ V jumps. The critical voltage slightly increases from $U_c = 1.22$ V at $x = 0.01$ to $U_c = 1.25$ V for $x = 0.05$. The jump in the I–V characteristic shifts toward stronger electric fields: $U_c = 1.26$ V at $x = 0.01$ and $U_c = 1.43$ V at $x = 0.05$ V in the magnetic field $H = 8$ kOe. The magnetoresistive effect grows with concentration and amounts to 4% at $x = 0.01$, 10% at $x = 0.03$, and 16% at $x = 0.05$ (Fig. 8b, d, and f). The electric field polarity variation in a magnetic field causes the critical voltage shift $(U_c(H) - U_c(-H))/U_c(H) = 0.05$ and a decrease in the magnetoresistance by a factor of 2 for the composition with $x = 0.03$. As the temperature is increased, the magnetoresistive effect enhances and at $T = 400$ K the magnetoresistance amounts to 14%. The current dependence of magnetoresistance was established and a broad maximum was observed (Fig. 8d and f).

At the voltages $U < U_c$, the experimental data are satisfactorily described by the I–V characteristics for Schottky diodes in the backward direction $I = I_0(\exp(qU/nkT) - 1)$ [24], where I_0 is the saturation current and n is the nonideality coefficient. In our systems with charge ordering, we change

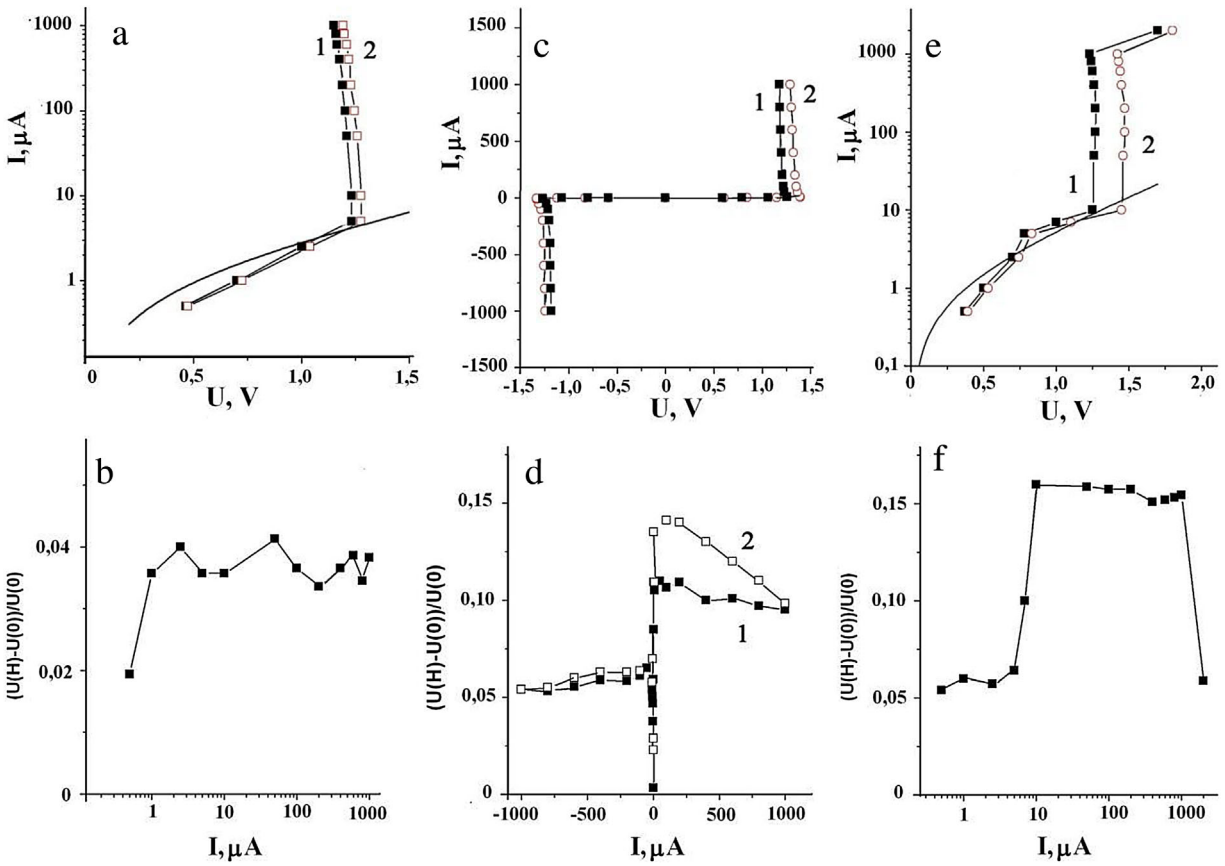

Figure 8 I–V characteristics for the $Ce_xMn_{1-x}S$ sample measured in zero magnetic field (1) and in the magnetic field $H = 8$ kOe (2) for $x = 0.01$ (a), 0.03 (c), and 0.05 (e) at room temperature. Voltage (resistivity) in a magnetic field versus dc current for $x = 0.01$ (b), 0.03 (d), and 0.05 (f) at $T = 300$ and 400 K (2–d). The fitting function $I = I_0\exp(N(E_c)U/kT)$ is shown by the solid line.

the charge value for charge density $N(E_c)$ at the carrier mobility edge $I = I_0(\exp(N(E_c)U/kT) - 1)$.

The external electric field causes redistribution of the spectral density of states and an increase in the electron (hole) density at the mobility edge by a factor of 3–5, depending on composition. This can result from the Fermi-energy shift toward the mobility edge by (20–30)%. The *I–V* characteristic is symmetric relative to the zero point, which is also explained within the orbital-charge ordering model. The excess electric charge density is located in the *xy*, *zx*, and *yz* planes, according to the symmetry of wave functions of the t_{2g} electron states. In an electric field, the polarization vector turns along the field direction and the spectral density changes correspondingly. For instance, charge redistribution from the *zx* to *xy* plane will lead to the change in the orbital angular momentum in a magnetic field and an increase in the critical voltage at which the Fermi level shifts to the mobility edge. The competition between the orbital angular momenta in a magnetic field and polarization of electric charges in an electric field causes the occurrence of maxima in the voltage dependence of magnetoresistance.

We determine the carrier sign in the temperature range $100\,\mathrm{K} < T < 450\,\mathrm{K}$ using the Hall effect. Hall coefficient measurements were performed on rectangular samples using a four-contact method, DC in a magnetic field 8 kOe. At measuring of the Hall coefficient the contributions of parasitic emf resulting from adverse galvanomagnetic and thermomagnetic effects were taken into account by measuring the voltage without a magnetic field and in a magnetic field. The difference between them is used for calculation of the Hall coefficient. Figure 9 shows the Hall coefficient R_x for the three compositions as a function of temperature. The Hall coefficient is negative in the temperature range $150\,\mathrm{K} < T < 377\,\mathrm{K}$ for $x = 0.01$ and has two pronounced minima at $T = 195$ and 340 K, which correspond to the magnetoresistance extrema (Fig. 7). As the concentration is increased, the electron conductivity region decreases to $200\,\mathrm{K} < T < 330\,\mathrm{K}$ and the $R_H(T)$ minimum is observed at $T = 284\,\mathrm{K}$, where the magnetoresistance changes its sign from negative to positive. Upon heating, $R_H(T)$ passes through the maximum at $T = 394\,\mathrm{K}$ and through the minimum at $T = 442\,\mathrm{K}$ (Fig. 9) for the composition with $x = 0.03$. For the composition with $x = 0.05$, the temperature of the maximum Hall coefficient $T = 327\,\mathrm{K}$ (Fig. 9b) coincides with the temperature of the magnetoresistance maximum (Fig. 7). Below the crossover temperature at which hopping conductivity changes for tunnel 1, the Hall coefficient decreases by more than an order of magnitude. At the same Hall factor value for electrons and holes, the Hall coefficient for semiconductors is [25]

$$R_H = \frac{\left(p\mu_p^2 - n\mu_n^2\right)}{e\left(p\mu_p + n\mu_n\right)^2} = \frac{e\left(p\mu_p^2 - n\mu_n^2\right)}{\sigma^2}, \qquad (3)$$

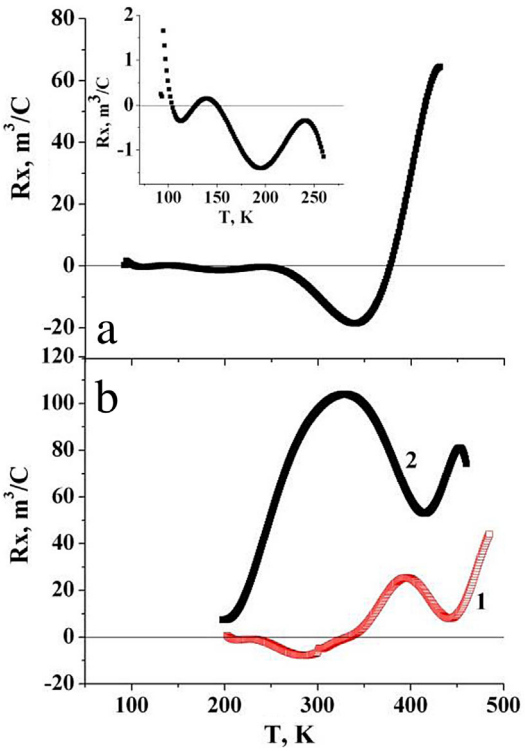

Figure 9 Temperature dependence of the Hall coefficient measured in the magnetic field $H = 8\,\mathrm{kOe}$ perpendicular to the current for the $Ce_xMn_{1-x}S$ samples with $x = 0.01$ (a), 0.03 (b, (1)), and 0.05 (b, (2)). Inset: temperature dependence of the Hall coefficient in the magnetic field $H = 8\,\mathrm{kOe}$ for $x = 0.01$ in the temperature range 50–280 K.

where $\mu_{p,n}$ is the hole and electron mobility; p and n are the hole and electron concentrations, respectively; and σ is the conductivity. In the temperature range 100–200 K, a decrease in the Hall coefficient is caused by an increase in conductivity σ, which is higher by several times than that at room temperature. The carrier sign change for the compositions with $x = 0.01$ and 0.03 is caused by the carrier mobility variation at low temperatures and by an increase in hole concentration at high temperatures.

For the composition with $x = 0.05$, the main contribution to the conductivity is made by holes; therefore, the hole concentration and mobility of carriers with isotropic effective masses can be estimated from $R_H = 1/ep$, $\sigma = ep\mu_p$ using the free electron gas model. Figure 10b shows that the mobility of holes exponentially increases in the range $200\,\mathrm{K} < T < 300\,\mathrm{K}$ with the activation energy $\Delta E = 0.15\,\mathrm{eV}$ and acquires its maximum value at $T = 360\,\mathrm{K}$. Hole concentration exponentially decreases with $\Delta E = 0.18\,\mathrm{eV}$ and has its minimum at $T = 340\,\mathrm{K}$ and a maximum at $T = 415\,\mathrm{K}$ (Fig. 10). A decrease in the hole concentration can be interpreted as partial recombination of electrons with holes. It should be noted that the interaction between carriers can lead to qualitatively different results.

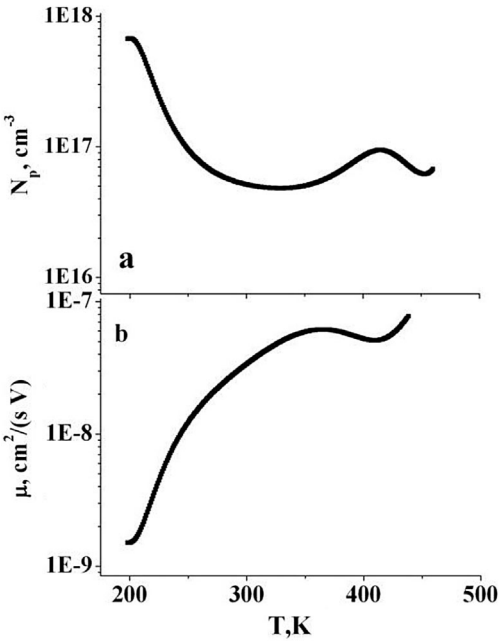

Figure 10 Concentration (a) and mobility (b) of electrons in $Ce_{0.05}Mn_{0.95}S$ versus temperature.

5 Conclusions Substitution of cerium for manganese ions in the $Ce_xMn_{1-x}S$ solid solutions leads to the deviation of magnetic susceptibility from the Curie–Weiss law and to its decrease upon cooling below 500 K in a magnetic field. Electron doping leads to degeneracy of the t_{2g} states of manganese ions, which is eliminated by the Coulomb interaction. The electronic structure variation on the manganese ion induces strain or rotation of sulfur octahedra and partial localization of holes, which leads to the variation in the exchange coupling value and to the magnetic susceptibility anomaly.

The dependence of inductance (magnetic permeability) to the measurement conditions of the sample cooled in zero and nonzero fields in the range 230–270 K and below the Nèel temperature was established. In the sample cooled in a magnetic field, the inductance and Q-factor jumps in the magnetically ordered phase were observed. The anomalies in the temperature dependence of the inductance and Q factor of electromagnetic oscillations of the coil with the sample below the Néel temperature in a magnetic field are caused by the spin–orbit interaction and rearrangement of the orbital and spin structures, while at higher temperatures, they result from elimination of degenerate orbital states in a magnetic field.

For all the investigated $Ce_xMn_{1-x}S$ compositions ($0.01 \le x \le 0.05$), the sample permittivity variations with temperature upon cooling with and without a field were found. The permittivity increases in a magnetic field and has a peak in the temperature range 440–470 K, which shifts toward higher temperatures in a magnetic field. The dependence $\varepsilon(T)$ is described within the model of electron localization, which vanishes above 470 K. The dielectric loss is described using the Debye model with a relaxation frequency of about 10 MHz at low temperatures; the temperature of the maximum dielectric loss also shifts to the high-temperature region in a magnetic field. In the magnetically ordered state, the dielectric loss is enhanced by the magnetic field and changes its sign above the Néel temperature. An increase in the dielectric loss in a magnetic field below the Néel temperature is associated with the spin–orbit interaction, since the wave vector of orbital correlations changes upon sample cooling in the FC mode. In this case, the dielectric loss is determined by the magnetoelectric interaction and energy transfer to the magnetic subsystem.

In the $Ce_xMn_{1-x}S$ solid solutions an enhancement of the magnetoresistive effect on increasing the degree of cationic substitution is found. The correlation of change in the sign of the magnetoresistance and the type of current of carriers versus temperature is established. For the two investigated compositions ($x = 0.01$ and 0.03), the temperature range of the electron-type conductivity is determined; for the composition with $x = 0.05$, the hole-type conductivity is observed. The hole concentration and carrier mobility for composition $x = 0.05$ are estimated. The maximum of the magnetoresistivity for this composition is due to the maximum of the mobility hole.

The model of charge-orbital ordering of electrons was proposed. Below 500 K, the carriers are in the bound state and electrons in the t_{2g} states form the spin-glass-like orbital order. As the temperature is decreased, the energy levels of the occupied t_{2g} states split in the system with strong electron correlations. This degeneracy is eliminated in a magnetic field at the interaction with the electron angular momentum.

Acknowledgments This work was financially supported by RFFI no. 15-42-04099 r_sibir_a, RFFI no. 16-52-00045 Bel_a, and government work no. 114090470016.

References

[1] A. Fert, Rev. Mod. Phys. **80**, 1517 (2008).
[2] D. Awschalom, Spin Electronics (Kluwer Academic Publishers, Dordrecht, Boston, 2004).
[3] R. Peters and N. Kawakami, Phys. Rev. B **83**, 125110 (2011).
[4] P. Werner, E. Gull, M. Troyer, and A. J. Millis, Phys. Rev. Lett. **101**, 166405 (2008).
[5] S. S. Aplesnin and A. I. Moskvin, J. Phys.: Condens. Matter **20**, 325202 (2008).
[6] M. De Raychaudhury, E. Pavarini, and O. K. Andersen, Phys. Rev. Lett. **99**, 126402 (2007).
[7] P. A. Kumar, R. Mathieu, P. Nordblad, S. Ray, O. Karis, G. Andersson, and D. D. Sarma, Phys. Rev. X **4**, 011037 (2014).
[8] K. I. Kugel, A. L. Rakhmanov, A. O. Sboycha, and D. I. Khomskii, Phys. Rev. B **78**, 155113 (2008).
[9] S. S. Aplesnin, L. I. Ryabinkina, O. B. Romanova, D. A. Velikanov, A. D. Balaev, D. A. Balaev, K. I. Yanushkevich, A. I. Galyas, and O. F. Demidenko, JETP **106**, 765 (2008).

[10] S. S. Aplesnin, O. N. Bandurina, O. B. Romanova, L. I. Ryabinkina, A. D. Balaev, and E. V. Eremin, J. Phys.: Condens. Matter **22**, 226006 (2010).
[11] S. S. Aplesnin, L. I. Ryabinkina, G. M. Abramova, O. B. Romanova, A. M. Vorotynov, D. A. Velikanov, N. I. Kiselev, and A. D. Balaev, Phys. Rev. **71**, 115103 (2005).
[12] S. H. Kan, I. Felner, and U. Banin, Isr. J. Chem. **41**, 55 (2001).
[13] G. A. Alanko and D. P. Butt, J. Am. Ceram. Soc. **97**, 2357 (2014).
[14] R. Pittini, J. Schoenes, and P. Wachter, Phys. Rev. B **55**, 7524 (1997).
[15] P. Strange, A. Svane, W. M. Temmerman, Z. Szotek, and H. Winter, Nature **399**, 756 (1999).
[16] S. S. Aplesnin and M. N. Sitnikov, JETP Lett. **100**, 95 (2014).
[17] S. S. Aplesnin, L. I. Ryabinkina, O. B. Romanova, V. V. Sokolov, A. Yu. Pichugin, A. I. Galyas, O. F. Demidenko, G. I. Makovetskii, and K. I. Yanushkevich, Phys. Solid State **51**, 698 (2009).
[18] S. S. Aplesnin, M. N. Sitnikov, O. B. Romanova, E. V. Eremin, V. V. Sokolov, and A. Yu. Pichugin, Solid State Phenom. **233–234**, 419 (2015).
[19] Y. Mita, M. Kobayashi, S. Endo, and S. Mochizuki, J. Magn. Magn. Mater. **272–276**, 428 (2004).
[20] H. van der Heide, C. F. van Bruggen, G. A. Wiegers, and C. Haas, J. Phys. C **16**, 855 (1983).
[21] C. Aebischer, D. Baeriswyl, and R. M. Noack, Phys. Rev. Lett. **86**, 468 (2001).
[22] M. A. Alzamil, Res. J. Appl. Sci. Eng. Tech. **5**, 481 (2013).
[23] E. A. Eliseev, A. N. Morozovska, G. S. Svechnikov, E. L. Rumyantsev, E. L. Shishkin, V. Y. Shur, and S. V. Kalinin, Phys. Rev. B **78**, 245409 (2008).
[24] V. L. Bonch-Bruevich and S. G. Kalashnikov, Fizika poluprovodnikov (Nauka, Moscow, 1990), p. 672.
[25] N. Q. Bau and B. D. Hoi, Int. Ferroelectr. **155**, 39 (2014).